

Improving the Calibration Efficiency of X-ray Focusing Mirrors – Simulation and Experiment*

Yi-Fan Zhang,^{1,2} Zi-Jian Zhao,^{1,2} Yu-Xuan Zhu,¹ Vadim Burwitz,³ Xiong-Tao Yang,¹ Yan-Ji Yang,¹ Dong Xie,¹ Yu-Sa Wang,^{1,2,†} and Yu-Peng Xu^{1,2,‡}

¹Key Laboratory of Particle Astrophysics, Institute of High Energy Physics,
Chinese Academy of Sciences, Beijing 100049, China

²University of Chinese Academy of Sciences, Chinese Academy of Sciences, Beijing 100049, China

³Max Planck Institute for Extraterrestrial Physics, Giessenbachstr., 85748 Garching, Germany.

With the development of X-ray astronomy, X-ray focusing mirrors are evolving toward higher effective area, higher angular resolution, and larger fields of view. This introduces new requirements for the calibration of X-ray focusing mirrors. To efficiently and accurately complete the effective area measurements of the enhanced X-ray Timing and Polarimetry (eXTP) mission, we validated the feasibility of using the SDD detector, which provides high energy resolution and can operate under high photon flux conditions, for continuum effective area measurements. The feasibility of directly using the SDD for the measurements is first validated through Geant4. Subsequently, the method for aligning the SDD detector before the measurements is discussed. Later, the methods for dead-time correction and the calculation of measurement errors are considered. Finally, using the pnCCD as the detector, we measured the effective area of the eXTP 3-shells mirror module at different X-ray emission lines and compared these results with the effective area obtained by using the SDD detector for continuum measurements. The results showed that the deviation between the two methods was better than 3.6 %, and the trends in the varying effective area with energy were consistent.

Keywords: eXTP, Effective Area, SDD, Continuum

I. INTRODUCTION

As X-ray astronomy continues to evolve, the performance requirements for X-ray telescopes are also being enhanced, primarily in the areas of angular resolution, Effective Area (EA), and Field of View (FoV). As X-ray focusing mirrors undergo iterative improvements, new requirements for on-ground X-ray calibration have emerged. Taking the Spectroscopy Focusing Array (SFA) and Polarimetry Focusing Array (PFA) payloads of the enhanced X-ray Timing and Polarimetry (eXTP) mission as examples, nine sets of Wolter-I focusing mirror assemblies are employed to enable high-precision determination of neutron star mass and radius and to improve the signal-to-noise ratio for polarization observations[1]. The gradual increase in effective area and number of focusing mirror assemblies presents new challenges for traditional calibration methods.

Due to excellent imaging capabilities and energy resolution, Charge Coupled Devices (CCDs) are widely used in ground calibration of X-ray focusing mirrors[2, 3]. For CCDs, event acquisition involves reconstructing images from each exposure, and the readout of charges generated by photon deposition in the CCD requires per-pixel transfer. This process has several implications: firstly, in focused conditions where the flux is high, it is necessary to reduce the flux to prevent pile-up, which results in an extremely low flat-field intensity. This increases the time required to measure every focusing mirror assembly significantly. Given that X-ray tubes, which are commonly used as X-ray sources, have an output that varies over time, prolonged measurements can lead to

substantial increases in measurement errors. Secondly, the transfer of charge between pixels can result in charge loss, which causes tailing at the low-energy end. This limitation requires CCDs to use monochromatic fluorescence lines for measuring the effective area of focusing mirrors at individual energy points, which significantly increases the measurement time.

In 1997, the Chandra ground calibration team attempted to calibrate the effective area of focusing mirrors by using a high-energy resolution HPGe detector to measure the continuum[4, 5]. Because this detector needs to operate at low temperatures, the thickness of ice could affect the measurement results. We have now validated the feasibility of using SDDs to efficiently measure the effective area of X-ray optics by measuring the continuum in the 100-m X-ray test Facility (100XF)[6], and have presented simulation analyses and correction methods. Compared to the HPGe detector, the SDD can operate at -20°C without the risk of icing under vacuum conditions. In this paper, Section II details our testing and analysis methods. And simulation results are displayed in Section III. Finally, in Section IV experimental results are presented.

II. METHOD

It involves collecting the energy spectra with an SDD under both flat-field and focused conditions. By dividing the spectra at the same energy bins, and then multiplying by the area of the SDD and a point source correction factor, we can calculate the curve of effective area versus energy. The formula is shown in Eq. 1.

$$A_{\text{eff}}(E) = C_{\text{Correction}} A_{\text{Detector}} \frac{S_{\text{Focus}}(E)}{S_{\text{Flat}}(E)} \quad (1)$$

* Supported by the China's Space Origins Exploration Program

† Corresponding author, wangyusa@ihep.ac.cn

‡ Corresponding author, xuyup@ihep.ac.cn

Where $A_{\text{eff}}(E)$ is the effective area at energy E , $C_{\text{Correction}}$ is the point source correction factor, A_{Detector} is the geometric area of the detector, $S_{\text{Focus}}(E)$ is the focused count rate, and $S_{\text{Flat}}(E)$ is the flat-field count rate. The point source correction factor is derived by the inverse square relationship between the flux and the distance from the X-ray source, as shown in Eq. 2.

$$C_{\text{Correction}} = \frac{D_{\text{Mirror}}^2}{D_{\text{Detector}}^2} \quad (2)$$

Where D_{Mirror} is the distance from the focusing mirror to the X-ray source, and D_{Detector} is the distance from the SDD used to measure the effective area to the source.

III. SIMULATION

For current SDDs, a good energy response has been achieved. However, subtle effects such as incomplete charge collection, escape peaks, and detector energy broadening may result in some photons being recorded as other energies, as shown in Fig. 1. For example, for a photon with energy E , when it deposits energy and excites the silicon within the detector, forming a Si-K α line at 1.74 keV, and if the 1.74 keV photon leaves the sensitive area of the detector, then the photon at energy E will contribute to the effective area at $E-1.74$ keV. Incomplete charge collection and detector energy broadening can similarly introduce deviations in the measurement of the effective area.

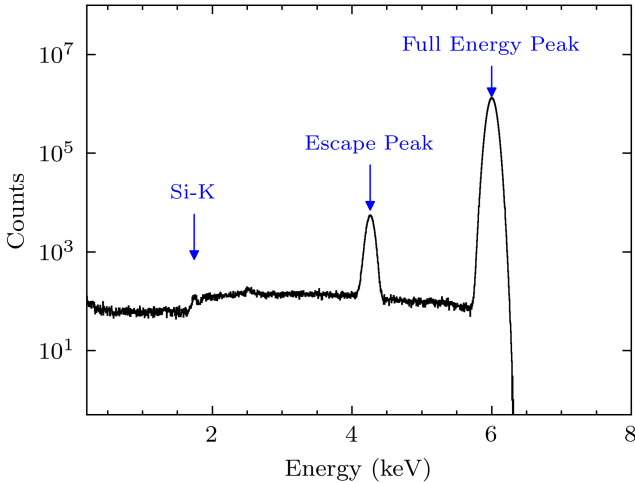


Fig. 1. The simulated response of the SDD at 6 keV. It includes the full-energy peak of 6 keV photons, the escape peak at 4.26 keV, the Si-K α emission line at 1.74 keV, and a continuum plateau resulting from incomplete charge absorption effects.

To verify the feasibility of the method, a series of Monte Carlo simulations were conducted. The X-ray source and detector were simulated using Geant4, with electromagnetic interactions handled by the ‘EM Pen’ electromagnetic physics

constructors, and fluorescence lines generated from the ‘fluorBearden’ library. In actual experiments, X-ray tubes are commonly used as the X-ray source. To achieve spectral consistency, copper (Cu) alloyed with 0.4 % silicon (Si) and 1.7 % molybdenum (Mo) was used as the X-ray tube’s target material in subsequent simulations. The detector geometry was modeled according to the actual dimensions, including a 450 μm thick active volume, a collimated diameter of 10.5 mm, and a 25.4 μm thick Be window. The detector’s broadening at a single energy point is calculated using Eq. 3.

$$FWHM(E) = 2.355\sqrt{aE + b} \quad (3)$$

Where a and b are constants. We determine the values of a and b by fitting the SDD energy resolution at the high-purity fluorescence lines produced by an X-ray secondary multi-target source[7]. The results are shown in Fig. 2.

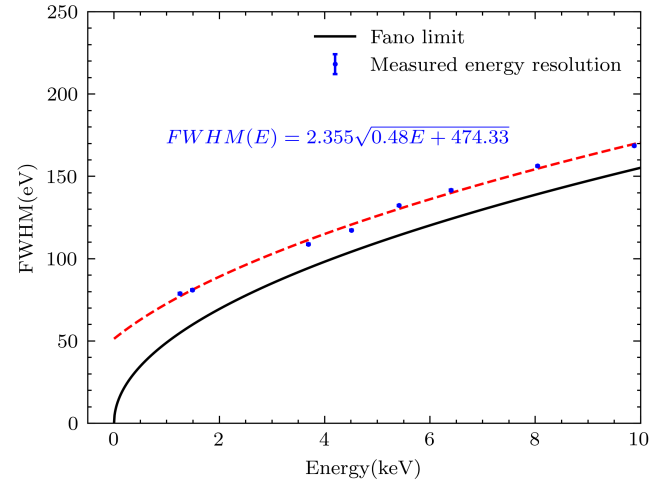


Fig. 2. Energy resolution at different fluorescence lines. Mg-K α (1.25 keV), Al-K α (1.49 keV), Ca-K α (3.69 keV), Ti-K α (4.51 keV), Cr-K α (5.41 keV), Fe-K α (6.40 keV), Cu-K α (8.04 keV), Ge-K α (9.88 keV) were used to measure the detector’s energy response.

The response of the focusing optics was determined based on the reflectivity data provided by The Center for X-Ray Optics (CXRO). The spectrum emitted by the copper-target X-ray tube was extracted from Geant4 as the flat-field spectrum. This spectrum was then multiplied by the corresponding effective area to derive the focused spectrum. In the detector simulation, both the flat-field spectrum and the focused energy spectrum were sampled as inputs to the detector. The resulting detector response spectrum and effective area are presented in Fig. 3.

According to the simulation results, dividing the focused spectrum by the flat-field spectrum can restore the effective area across most energy ranges. However, noticeable distortions occur in the low-energy region below 1.0 keV, around 6.3 keV, and near 8.0 keV. To identify the sources of deviation, each photon in the spectra for both the flat-field and focused states was tracked step-by-step. The energy of photons

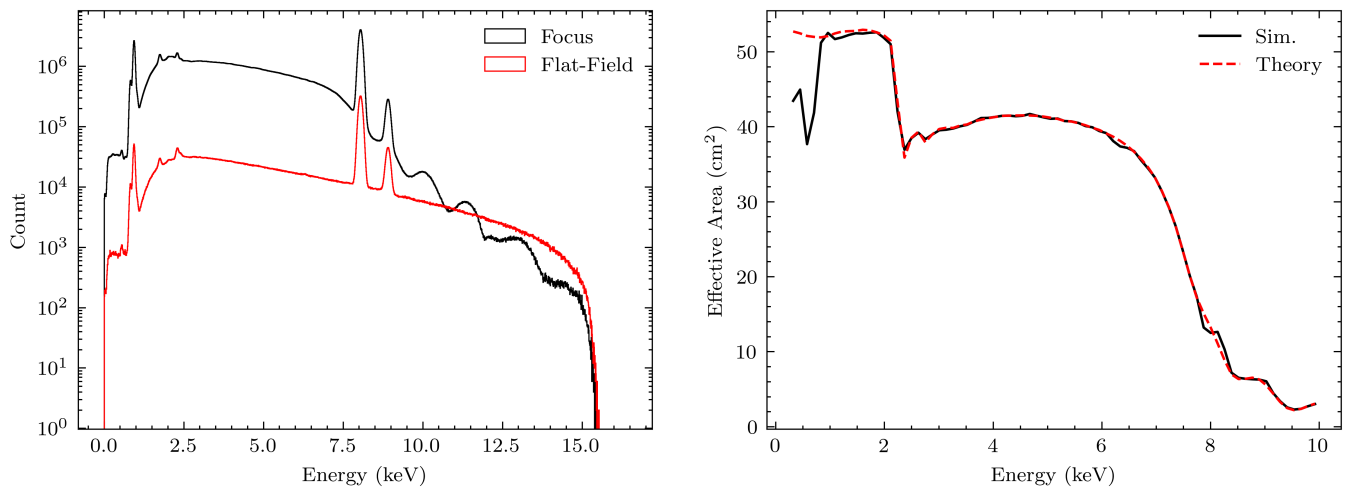


Fig. 3. Left Panel: Simulated Cu spectra for flat-field and focused conditions. Right Panel: The ideal input effective area curve and the simulated effective area curve.

before entering the detector, the energy deposited by photons within the detector, and the energy channels which they fell after energy broadening were recorded. The results are presented in Fig. 4.

The top of Fig. 4 displays the input spectra and the unbroadened deposition energy spectra for both flat-field and focused states. It also calculates the proportion of photons in the deposition energy spectra whose initial input energies do not fall within the same energy channel. Additionally, the effective areas derived from both the input spectra and the deposition energy spectra are calculated.

The results show that starting from 1.4 keV, as the energy decreases, the transmission of photons is progressively reduced due to the detector window, resulting in most of the low-energy photon counts being contributed by the incomplete absorption or escape of high-energy photons. Below 0.8 keV, the counts in the deposition spectra are completely from high-energy photons. At 0.9 keV, near the Cu-L emission line, the proportion of non-local energy decreases due to the strong intensity of the emission line. Additionally, due to the high count rate of Cu-K α , an increase in the non-local energy proportion occurs at 6.3 keV due to its escape peak. As for Cu-K β , its counts are about one order of magnitude lower than that of Cu-K α , the effect of its escape peak is negligible.

The effective area curves calculated from the input spectrum and the deposition spectrum demonstrate the impact of these effects on effective area measurement. The effective area calculated from the input spectrum is consistent with the theoretical effective area. However, the effective area calculated from the deposition spectrum shows a drop at 6.3 keV, as the photons at 6.3 keV actually include photons originally there and those escaping from the 8.0 keV Cu-K α emission line. Therefore, the effective area there is a weighted average of the effective areas at 6.3 keV and 8.0 keV. The lower effective area at 8.0 keV causes the dip at 6.3 keV. For photons with energies below 1.4 keV, the effective area gradually decreases due to the increasing contribution from high-energy

photons, whereas at 0.9 keV, the effective area approaches the theoretical value due to the increase in local photon counts, forming a drop structure in the effective area. For the energy range below 0.8 keV, the absence of local photons leads to a drop in the effective area.

The bottom of Fig. 4 displays the input and broadened spectra for both flat-field and focused states, the non-local energy ratio in the broadened spectra, and the effective area calculated from both spectra.

Compared to the unbroadened spectra, the non-local energy ratio in the broadened spectra increases with energy due to the gradual increase in energy resolution. Additionally, protrusions in the non-local energy ratio appear on either side of the characteristic peaks as a result of broadening. As shown in Fig. 5, for input photon energies of 8.0 keV and 8.9 keV, broadening results in significant contributions to the nearby 2-3 energy channels. This leads to distortions in the effective area calculated from the broadened deposition spectrum near 8.0 keV and 8.9 keV. For example, at 7.9 keV, 81 % of the total counts are due to broadening from 8.0 keV photons, resulting in a calculated effective area that is lower than the theoretical value. Similarly, at 8.1 keV, the effective area is higher than the theoretical value. For non-local energy increases caused by energy resolution, the effects of high-energy photon broadening often counteract the effects of low-energy photon broadening, leading to an effective area calculation that matches the theoretical value. Additionally, low-energy emission lines, such as Si-K α , have little impact on the measurement of the effective area due to their low intensity as impurities, the small broadening in their energy region, and the minor changes in the effective area. Therefore, their broadening effect can be neglected.

To reduce the impact of target material emission line broadening on the effective area, we used a combination of a polynomial function and a Gaussian function to fit the photon counts contributed by the emission lines and the bremsstrahlung continuum, respectively. The effective area

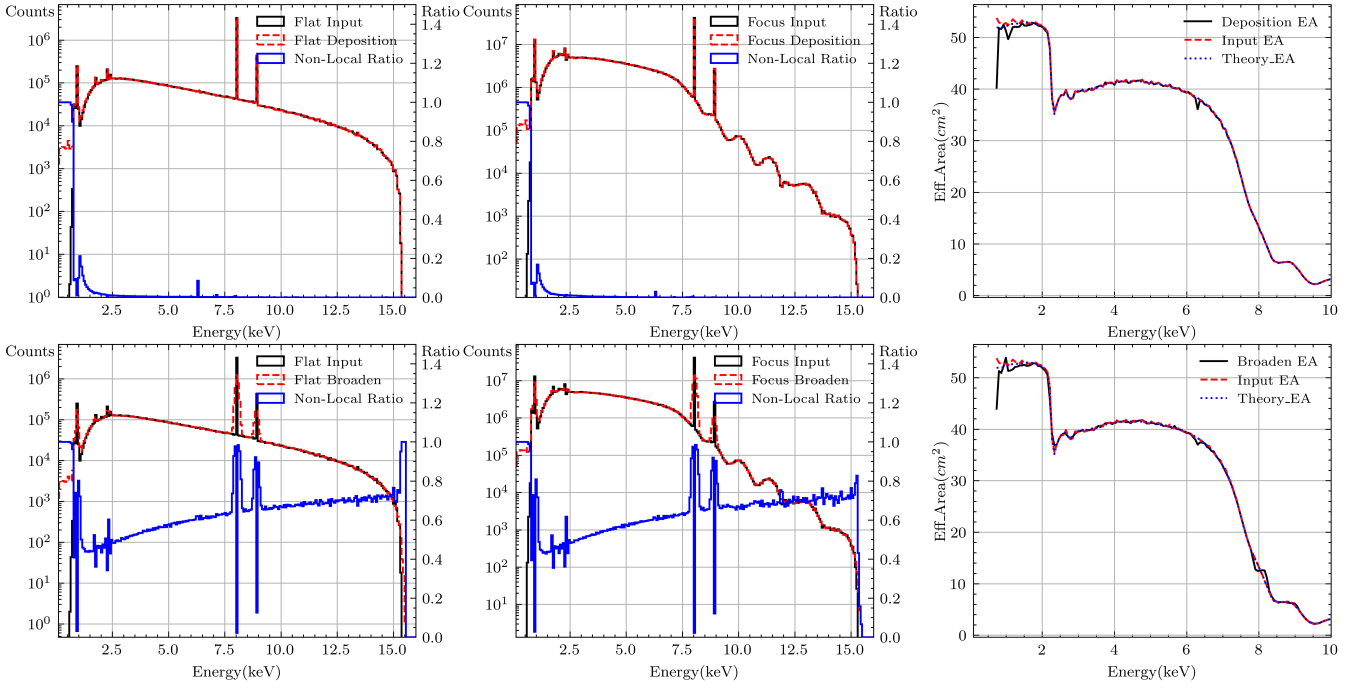


Fig. 4. Top-left panel: Flat-field input and deposition spectra, along with the proportion of non-local energy in the deposition spectrum. Top-middle panel: Focused input and deposition spectra, along with the proportion of non-local energy in the deposition spectrum. Top-right panel: Theoretical effective area and the effective area calculated from the input and deposition spectra. Bottom-left panel: Flat-field input and broadened spectrum, along with the proportion of non-local energy in the broadened spectrum. Bottom-middle panel: Focused input and broadened spectrum, along with the proportion of non-local energy in the broadened spectrum. Bottom-right panel: Theoretical effective area and the effective area calculated from the input and broadened spectrum.

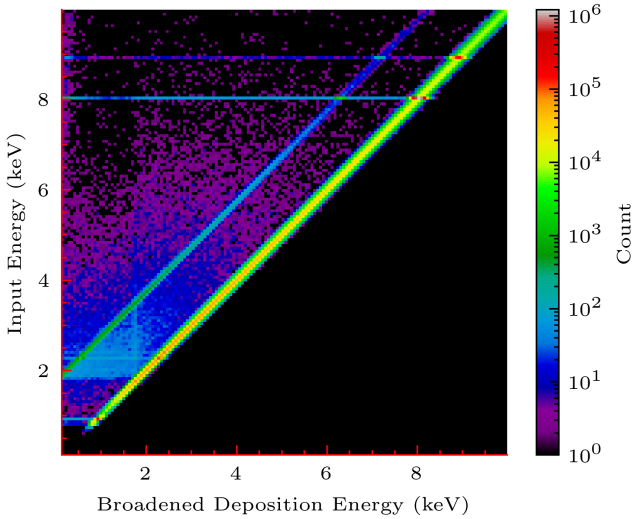


Fig. 5. The energy of input photon counts contributing to each energy channel of the broadened deposition spectrum under flat-field conditions.

curve at the Cu-K α escape peak, resulting in a deviation of 2.4% in the effective area. Since this occurs at the Fe-K α emission line, the effective area here can be supplemented by monochromatic point measurements.

IV. MEASUREMENT AND RESULT

A. Alignment

Since SDD is a non-imaging detector, it is necessary to study its alignment methods when used for measuring focusing mirrors. Before aligning the SDD, we first perform the alignment using a pnCCD named as the Color X-ray Camera (CXC)[8]. The alignment of the CXC includes two operations: axis alignment (scanning axis) and focus finding (scanning focus). Axis alignment is conducted by measuring the counts at different deflection angles along two orthogonal axes. The count values measured at different angles are fitted with a quadratic polynomial, and the angle corresponding to the maximum count is considered to be the direction of the optical axis. To determine whether the detector is at the focal point, we scan along the optical axis and fit the position where the Half Power Diameter (HPD) is minimized. A typical CXC scan result is shown in Fig. 7.

After completing the alignment with the CXC, the relative position of the detector is used to achieve the initial alignment

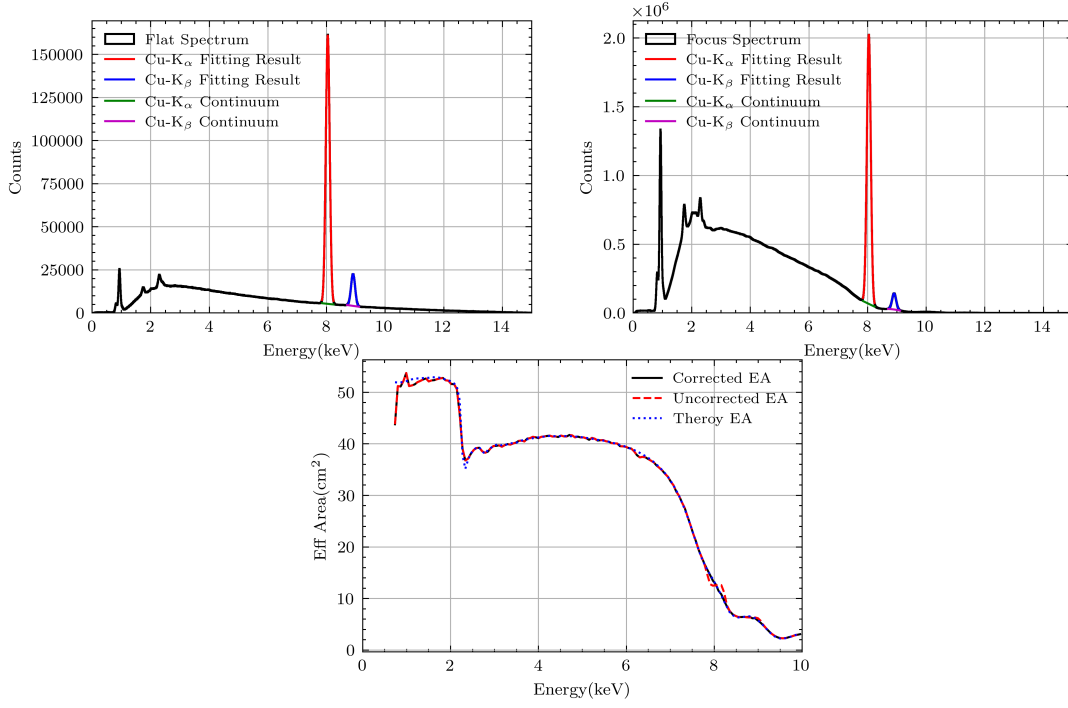


Fig. 6. Upper-left panel: Flat-field spectrum and corrected results for the Cu-K peaks; Upper-right panel: Focused spectrum and corrected results for the Cu-K peaks; Lower panel: Calculated effective area curves before and after correction, alongside the theoretical effective area curve.

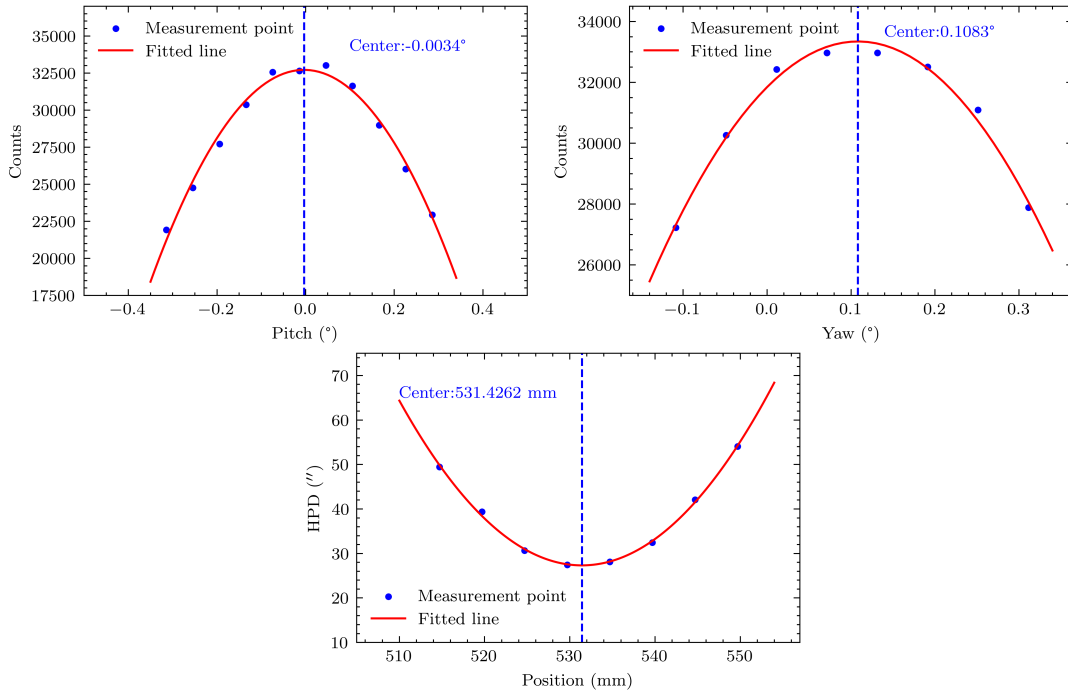


Fig. 7. Scan results along the pitch (top left), yaw (bottom right), and axial (bottom) directions. A quadratic polynomial is used to fit the scan points to locate the positions of maximum flux intensity and minimum HPD.

of the SDD. Subsequently, the SDD is scanned along two or- the optical axis, using variations in counts to locate the beam
thogonal axes on a common plane which is perpendicular to spot at the center of the detector. Fig. 8 displays a typical set

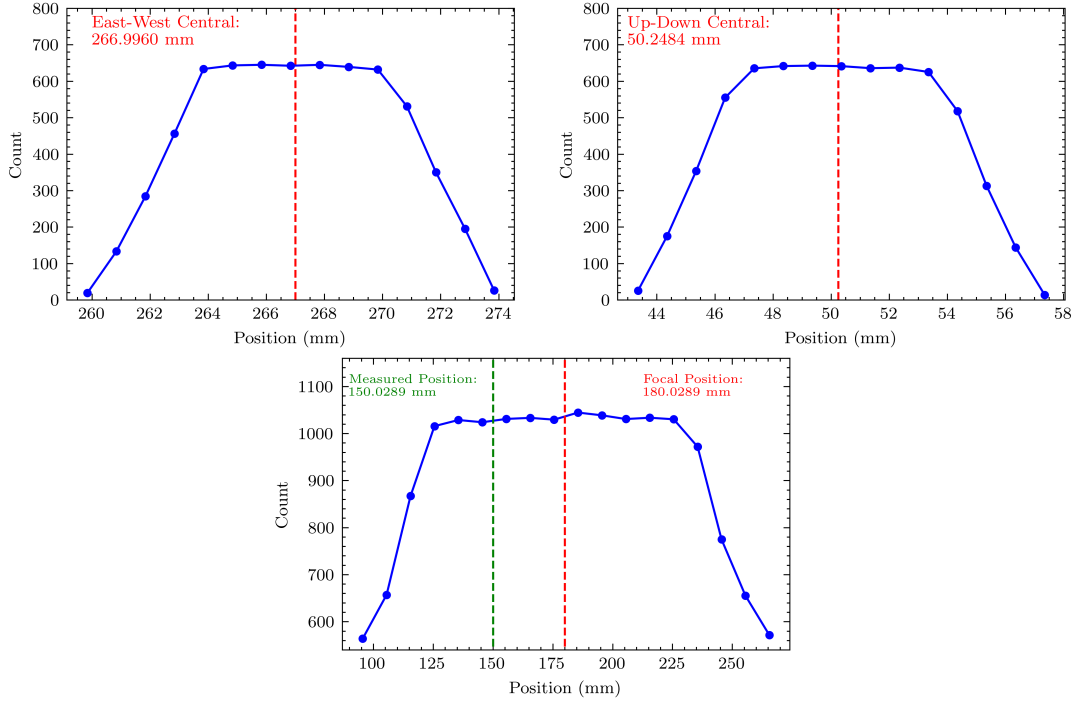


Fig. 8. The results of the SDD scans in three directions. For the two directions perpendicular to the optical axis, the plateau width is close to the diameter of the detector. Along the optical axis, there is no significant change in counts within a defocus range of approximately ± 50 mm.

of measurement results. Given our detector size (10.5 mm after collimation), a plateau which is about 10 mm wide is formed. We calculate the centroid of each scan, use the count values at different positions as weights, and use the centroid position as the location of the SDD.

The SDD detector was also scanned axially, as shown in the bottom panel of Fig. 8. The results indicate that there is no significant loss of counts at a defocus of approximately 50 mm. The detector used in the tests was equipped with a uniform Be window; however, to minimize the effects of window non-uniformity, measurements were performed at a defocus of 30 mm.

B. Dead Time Correction

According to the previous simulation results, it can be demonstrated that ignoring the energy response of the detector, the effective area measurement for the majority of the energy bands of the focusing mirror is accurate. However, the varying responses of the detector system due to flux still require analysis.

For the detector system, when multiple photons are detected in a short time, due to the time required by the electronics to process each photon, some photons cannot be processed within this time interval. As a result, the actual number of detected photons will be less than the number of photons depositing energy in the detector. This loss of photons is called “dead time losses”.

For the effective area measurement of focusing mirrors,

when measuring the flat-field spectrum, the photon flux is relatively low, resulting in fewer lost photons. However, during measurements with the focusing mirror, the flux is higher, leading to more photon losses. Consequently, the number of photons detected in each channel under focused conditions is smaller than the actual number of photons, which causes the effective area values across the full spectrum to be underestimated. Therefore, it is necessary to study the method for dead time correction in the detector system.

In the detector system we use, the output signal of the detector is passed into a digital signal processing module for analysis. After the signal is converted into a digital signal through an ADC, it is filtered by two trapezoidal filters with different shaping times, respectively. The filter with a short shaping time is referred to as the trigger filter, and it generates a dead time of approximately $0.2 \mu\text{s}$ per photon. The filter with a long shaping time is called the energy filter, which produces a dead time of approximately $8.3 \mu\text{s}$ per photon. The trigger filter is used to count the number of photons entering the detector and to discard certain photons in the energy filter based on the time intervals between consecutive photons. Due to its longer shaping time, the energy filter is used to evaluate the signal amplitude and generate the spectrum.

The number of photons recorded by the trigger filter is referred to as the measured input count rate, denoted as ICR_m . Since the width of the trigger filter’s output signal is used to determine whether the trigger filter itself experiences pulse pile-up, the relationship between the true input count rate (ICR_t) and the measured input count rate of the trigger filter follows a paralyzable dead-time model, which can be ex-

pressed by Eq. 4.

$$ICR_m = ICR_t \times e^{-ICR_t \times \tau_{df}} \quad (4)$$

Here, τ_{df} represents the dead time generated by the trigger filter for each photon. For our detector, this value is $0.2 \mu s$. From Eq. 4, the relationship between the output count rate of the trigger filter and the actual incident photon count rate can be plotted, as shown in Fig. 9. According to calculations, when $ICR_t = 10000$, the deviation between ICR_m and ICR_t is less than 0.2%. During the test, we typically ensure that the count rate in the focused condition is less than 5000 cps. Therefore, ICR_m can be considered equal to ICR_t . Based on this, we discuss the method for dead-time correction for each channel of spectra. The dead time loss is independent of energy, so the following relationship can be obtained:

$$\begin{aligned} \frac{N_{ti}}{N_{mi}} &= \frac{ICR_t}{OCR} \approx \frac{ICR_m}{OCR} \\ N_{ti} &= N_{mi} \times \frac{ICR_m}{OCR} \end{aligned} \quad (5)$$

Here, N_{ti} represents the true count for the i -th channel, N_{mi} represents the measured count for the i -th channel of the energy spectrum, and OCR is the output count rate of the energy filter. The values on the left side of Eq. 5 are measurable parameters. Using this equation, spectra under different flux conditions can be normalized to actual incident spectra.

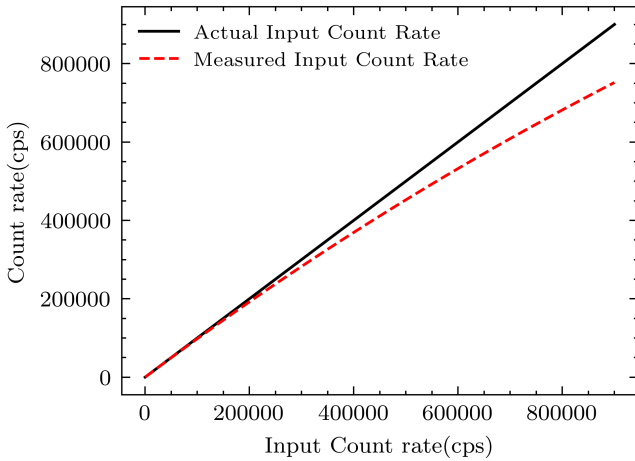


Fig. 9. The deviation of the trigger filter output count rate from the actual input count rate. When the actual count rate is not high, the output count rate of the fast trigger filter can effectively estimate the true input count rate.

Based on the method described in Section II, we measured the effective area of shells #21 and #22 of eXTP Mirror Module 3 (MM3) using continuum X-rays generated by electron bombardment of a copper target. eXTP-MM3 is a typical Wolter-I type mirror module, which includes the #1 shell from the outermost layer and the #21 and #22 shells from

the middle layer. The parameters of the mirrors are shown in Table 1.

Table 1. Design parameter of eXTP-MM3.

Shell#	R_{max} (mm)	R_0 (mm)	R_{min} (mm)
1	240.36	237.00	226.82
21	171.67	169.27	162.00
22	168.77	166.41	159.26

During this measurement, the focused count rate was 2968 cps, and the flat-field count rate was 132 cps. A comparison of the effective area calculation results with and without dead-time correction was made, with the results and deviations from the simulation shown in Fig. 10. After applying the dead-time correction, the deviation was reduced by approximately 2%.

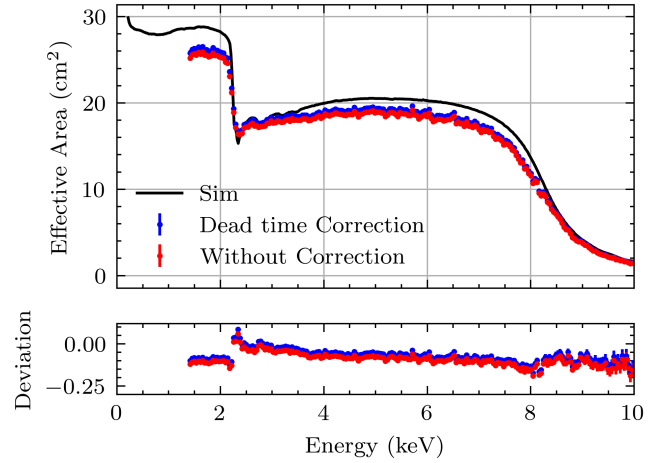


Fig. 10. Comparison of the effective area with and without dead-time correction. After applying the correction, the deviation of the calculated effective area from the simulation is reduced by 2% compared to the deviation without the correction.

C. Scattering correction

Due to the inevitable surface roughness of the actual focusing mirror, some photons are scattered by the mirror and cannot be focused onto the focal position. Therefore, in this study, a 3×3 array imaging scan was carried out at the defocus distance of 30 mm using the CXC, with the results shown in Fig. 11. Each pixel of the CXC is a square with a side length of $48 \mu m$, and the total pixel array is 268×268 . The scanning step size was set to 12.6 mm, which is approximately equal to the side length of the CXC. According to the statistics of the photon count ratio within the effective area of the SDD detector, about 96% of the photons can be effectively detected. On this basis, the measured effective area should be corrected using this scaling factor.

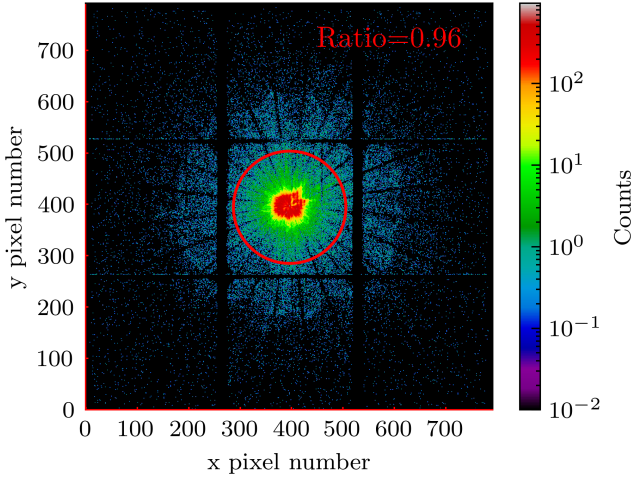


Fig. 11. Schematic of the measured spot at 30 mm defocus, together with the position and size of the SDD. The SDD collects 96 % of the total photons.

D. Error Calculation

The error for each channel is derived through the propagation of statistical errors. Assuming that photon counting follows a Poisson distribution, the error in photon count rates under flat-field and focused conditions can be expressed as:

$$\sigma_{S_{\text{Focus}}}(E) = \frac{\sqrt{\text{cnt}_{\text{Focus}}(E)}}{T_{\text{Focus}}} \quad (6)$$

$$\sigma_{S_{\text{Flat}}}(E) = \frac{\sqrt{\text{cnt}_{\text{Flat}}(E)}}{T_{\text{Flat}}} \quad (7)$$

Here, $\sigma_{S_{\text{Focus}}}(E)$ is the standard deviation of the count rate under focused conditions, and $\sigma_{S_{\text{Flat}}}(E)$ is the standard deviation of the count rate under flat-field conditions. $\text{cnt}_{\text{Focus}}(E)$ and $\text{cnt}_{\text{Flat}}(E)$ represent the counts in the channel E under focused and flat-field conditions, respectively. T_{Focus} and T_{Flat} are the measurement times for the focused and flat-field spectra, respectively. Considering Eq. 1, the measurement error of the effective area can be propagated as:

$$\sigma_{A_{\text{eff}}}^2(E) = C_{\text{Correction}}^2 A_{\text{Detector}}^2 \frac{S_{\text{Focus}}^2(E)}{S_{\text{Flat}}^2(E)} \times \left[\frac{\sigma_{S_{\text{Focus}}}^2(E)}{S_{\text{Focus}}^2(E)} + \frac{\sigma_{S_{\text{Flat}}}^2(E)}{S_{\text{Flat}}^2(E)} \right] \quad (8)$$

By replacing the count rate errors and count rates with counts and time, we get:

$$\sigma_{A_{\text{eff}}}(E) = C_{\text{Correction}} A_{\text{Detector}} \frac{T_{\text{Flat}}}{\text{cnt}_{\text{Flat}}(E)} \frac{\text{cnt}_{\text{Focus}}(E)}{T_{\text{Focus}}} \times \sqrt{\frac{1}{\text{cnt}_{\text{Focus}}(E)} + \frac{1}{\text{cnt}_{\text{Flat}}(E)}} \quad (9)$$

According to Eq. 9, when the flat-field count is constant, $\sigma_{A_{\text{eff}}}(E) \propto \sqrt{\text{cnt}_{\text{Focus}}(E)}$.

E. Results and Comparison

To validate the method, we used CXC to perform traditional effective area measurements of all three mirror shells of eXTP-MM3 at several emission line energies and we then compared the results with those obtained from continuum effective area measurements[9].

The continuum used in the measurements was generated by electron bombardment of a Cu target under a voltage of 16 kV. During the test, the detector's dead time was kept around 1 % (with the count rate of 1.2 kcps under the focused condition) to reduce the impact of count rate effects on the measurement results, such as dead time effect and pile-up. Additionally, due to the Be window in front of the detector, low-energy photons are absorbed. The proportion of events in the low-energy spectrum that are contributed by the incomplete absorption of high-energy photons increases. Therefore, this method shows distortion at the low-energy end, and we only compared measurement results above 1.4 keV. Moreover, we corrected the broadening of the Cu-K emission line. When attempting to correct for Cu-K β , the low photon counts and changes in effective area within the correction region could introduce additional deviation. Therefore, we performed corrections only for Cu-K α .

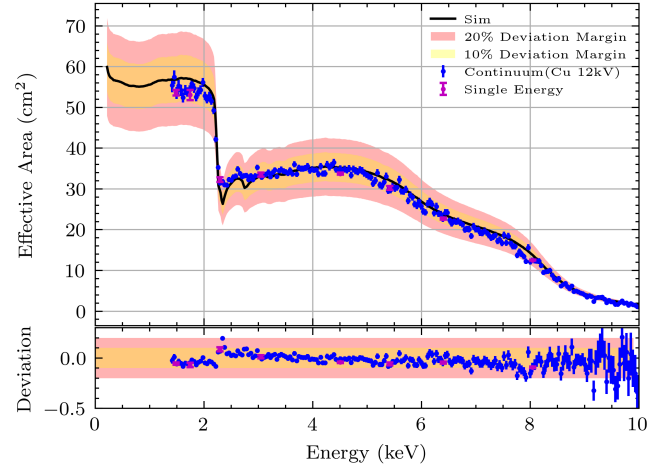


Fig. 12. Comparison of the continuum effective area test results with the traditional emission line effective area measurements. The results of the two measurement methods show a high degree of consistency, with a measurement deviation of less than 3.6 %.

As shown in Figure 12, the continuum effective area measurement results exhibit a high degree of consistency with the emission line effective area measurement results, with the maximum measurement deviation is less than 3.6 % and the average deviation of 1.5 %, which demonstrate the reliability of this method. Additionally, the measurement results from both methods were compared with the effective area values obtained through the specialized ray-tracing simulation[10].

This ray-tracing program takes into account factors such as divergence angles over the 100-meter testing process and the roughness of the focusing mirror. The deviations of both methods relative to the simulation values exhibited consistent trends, with the deviation remaining approximately 6%. Near the Au absorption edge, there is a noticeable variation in the deviation from the simulation. We currently consider this is related to carbon contamination or other behaviors of the focusing mirror.

V. SUMMARY

Due to the calibration requirements of multi-mirror, large-effective-area X-ray observatories such as eXTP, it is necessary to explore efficient and accurate methods for effective area calibration. Therefore, we tested using the SDD, which can obtain good energy resolution and can operate under high photon flux conditions within the 100XF to measure the effective area over a wide energy range using continua.

In this paper, we first verify the feasibility of the method through simulation and quantitatively evaluate the influence on the measurement results, such as incomplete absorption, escape peaks, and spectral broadening. Incomplete absorption is negligible in most energy ranges. However, for energies below 1.4 keV, the detector counts are almost entirely contributed by the incomplete absorption of high-energy photons due to the attenuation of low-energy photons by the Be window. Therefore, we consider that only data above 1.4 keV is reliable. The effect of escape peaks is also quantitatively evaluated. For measurements using the continua generated with a Cu target, combining the emission line measurement of Fe ensures that the effective area at the escape peak is correctly determined. The influence of spectral broadening is canceled out in the continuous spectrum. For emission peaks, we have developed a corresponding correction method. Then, we presented an alignment method for SDD, a non-imaging detector, in combination with the imaging pnCCD. Following that, we discussed how the dead-time effect and scattering influence the measurement results and provided a correction method, as well as the derivation of the effective area error. Finally, we compared the results of the continuum effective area measurement method with those of the traditional method, showing that the deviation between the two results is less than 3.6%. However, the former offers greater advantages due to its wider energy range in a single measurement

and shorter measurement time.

Author Contributions

Yifan Zhang and Zijian Zhao coauthored the paper and made equal contributions to this work. Yusa Wang and Yupeng Xu participated in the experimental design. Zijian Zhao, Xiongtao Yang and Dong Xie performed the experimental measurements. Yifan Zhang, Yuxuan Zhu, and Vadim Burwitz analyzed the experimental and simulation data. Yifan Zhang and Yuxuan Zhu respectively performed the detector and mirror simulations. All authors reviewed the manuscript and contributed to this work.

Acknowledgments

We would like to thank Liqiang Qi and Jingyu Xiao for their assistance with the Geant4 simulations.

DECLARATIONS

1. Conflict of interest

The authors declare that they have no conflict of interest.

2. Declaration of Generative AI Use

During the preparation of this work, the authors used Doubao for the purpose of language editing and grammar checking only. The tool was used to improve the readability and clarity of the text. After using this service/tool, the authors reviewed and edited the content as needed and take full responsibility for the content of the published article. No AI tool was used to generate scientific data, perform analysis, or formulate conclusions.

3. Data Availability Statement

The data that support the findings of this study are openly available in Science Data Bank at <https://cstr.cn/31253.11.sciencedb.j00186.01087> and <https://doi.org/10.57760/sciencedb.j00186.01087>.

- [1] S. N. Zhang, A. Santangelo, Y. P. Xu, *et al.*, The enhanced X-ray Timing and Polarimetry mission—eXTP for launch in 2030. *Sci. China Phys., Mech. & Astron.*, **68**: 119502 (2025). DOI: [10.1007/s11433-025-2786-6](https://doi.org/10.1007/s11433-025-2786-6)
- [2] K. Dennerl, R. Andritschke, H. Bräuninger, *et al.*, The calibration of eROSITA on SRG. In: *Space Telescopes and Instru-*

- mentation 2020: Ultraviolet to Gamma Ray, **11444**: 777–796 (2020). DOI: [10.1117/12.2562330](https://doi.org/10.1117/12.2562330)
- [3] P. Friedrich, V. Stieglitz, V. Burwitz, *et al.*, X-ray optics test and calibration of the Einstein Probe Follow-up telescope. *Acta Astronautica*, **221**: 255–265 (2024). DOI: [10.1016/j.actaastro.2024.05.016](https://doi.org/10.1016/j.actaastro.2024.05.016)

- [4] J. J. Kolodziejczak, R. A. Austin, R. F. Elsner, *et al.*, Uses of continuum radiation in the AXAF calibration. In: *Grazing Incidence and Multilayer X-Ray Optical Systems*, **3113**: 65–76 (1997). DOI: [10.1117/12.278889](https://doi.org/10.1117/12.278889)
- [5] P. Zhao, R. A. Austin, R. J. Edgar, *et al.*, AXAF-mirror effective area calibration using the C-continuum source and solid state detectors. In: *X-Ray Optics, Instruments, and Missions*, **3444**: 234–257 (1998). DOI: [10.1117/12.331240](https://doi.org/10.1117/12.331240)
- [6] Y.S. Wang, Z.J. Zhao, D.J. Hou, *et al.*, The 100-m X-ray test facility at IHEP. *Experimental Astronomy*, **55**: 427–445 (2023). DOI: [10.1007/s10686-022-09872-7](https://doi.org/10.1007/s10686-022-09872-7)
- [7] Y. X. Zhu, Y. Wang, Y. Chen, *et al.*, X-ray secondary multiple target sources for calibration of soft X-ray detectors. *Nuclear Techniques*, **44**: 39–44 (2021). (in Chinese) DOI: [10.11889/j.0253-3219.2021.hjs.44.050402](https://doi.org/10.11889/j.0253-3219.2021.hjs.44.050402)
- [8] D. Hou, Y. Wang, Z. Zhao, *et al.*, Characterization of a pnCCD-based Camera for Applications at the 100 m X-Ray Test Facility. *Publications of the Astronomical Society of the Pacific*, **135**: 064505 (2023). DOI: [10.1088/1538-3873/acdf20](https://doi.org/10.1088/1538-3873/acdf20)
- [9] Y.X. Zhu, V. Burwitz, D.J. Hou, Y.F. Zhang, Z.J. Zhao, X.T. Yang, Y.J. Yang, D. Xie, J. Ma, Y.S. Wang, *et al.*, Cross-calibration of an eXTP Mirror Prototype at 100XF and PANTER. *Publications of the Astronomical Society of the Pacific*, **137**(12): 125001 (2025). DOI: [10.1088/1538-3873/ae1fae](https://doi.org/10.1088/1538-3873/ae1fae)
- [10] Y.X. Zhu, Y.J. Yang, X.F. Zhao, J. Wang, T.X. Chen, Y.S. Wang, W.W. Cui, W. Li, D.W. Han, P. Friedrich, *et al.*, An X-Ray Optic System Ray-tracing Package for FXT on Board EP Satellite. *Publications of the Astronomical Society of the Pacific*, **137**(4): 045001 (2025). DOI: [10.1088/1538-3873/adc0c0](https://doi.org/10.1088/1538-3873/adc0c0)